# 6-DOF Outdoor High-Load Robot for Solar Panel Array Installation: Deformation Compensation, Inverse Kinematics and Decoupling Control

Shi Li [1,2]

[1.] The School of Intelligent Robotics and Advanced Manufacturing
Fudan University
Shanghai, China
[2.] Shanghai Bolightrobotics Co., Ltd.
Shanghai, China
s.lee@163.com

Xiaofeng Yang[*]
State Key Laboratory of ASIC and System
Fudan University
Shanghai, China
[*]xf_yang@fudan.edu.cn

*Abstract*—**The installation of modules in photovoltaic power plants remains largely manual, creating an urgent demand for automated solutions. Outdoor ground slopes and local unevenness cause equipment tilt and structural deformation, severely reducing end-effector (EE) positioning accuracy. This paper presents a 6-DOF outdoor high-load robotic system combining a 4-cable under-constrained cable-driven parallel robot (CDPR) with a multi-layer trolley mechanism, and introduces two key innovations: a mixed nonlinear interpolation (MNIP) algorithm to compensate structural deformation from terrain irregularities, and slope-aware inverse kinematics to incorporate ground slope effects into the CDPR model for improved EE accuracy. For the unique configuration, a piecewise decoupled motion workflow (PDMW) with real-time inverse kinematics reverse compensation (IKRC) enables precise 6-DOF decoupling control. Field tests at a desert site (slope <10°, local unevenness ≤0.5 m) installing an 800 kg solar panel array (SPA) achieved 0.03–0.05 m positioning accuracy and <0.2° angular deviation, validating the system's robustness and suitability for large-scale and high-load SPA installation.**

*Keywords- high-load robot, inverse kinematics, deformation compensation, cable-driven parallel robot control, decoupling control*

## I. INTRODUCTION

In recent years, with the increasing demand for electricity, numerous large-scale photovoltaic power plants have been constructed. Due to the complexity of outdoor environments, the handling and installation of photovoltaic modules are still mainly performed manually, which is inefficient and poses potential safety risks, leading to an urgent need for automated installation solutions. Cable-Driven Parallel Robots (CDPRs) have been widely applied in outdoor handling and installation tasks [1]–[3] owing to their advantages of large workspace, high load-to-weight ratio, and low cost [4], [5]. In [6], a large-scale cable robot with winches mounted on mobile towers is proposed for the on-site automatic installation of solar panels.

In these application scenarios, the operational accuracy of the EE is a core requirement. In [2], the CDPR achieved an absolute accuracy of 4 mm to 23 mm for curtain wall module installation, while [3] introduced a 3D concrete printer with a printing accuracy of approximately 1 cm. Therefore, improving the accuracy of cable-driven robots has become an important research focus [7].

The operational accuracy of CDPRs can be affected by various factors [8], such as cable elasticity, cable sagging, winch winding errors, and controller performance. In [9], a length model based on the characteristics of plastic fiber ropes reduced the average position deviation from 46.5 mm to 29.0 mm. In [10], the neglected effects of cable sagging and pulleys were considered to improve accuracy while expanding the workspace by 19.5%. In [11], a self-calibration framework was developed to explicitly address the cable sag effect. The works in [12], [13] accounted for the mass and elasticity of transmission cables and established a complete model for the CDPR of FAST, achieving the required accuracy.

Some studies have performed deviation correction based on winch or pulley characteristics: [14] analyzed the kinematic model of the winch–pulley mechanism and derived modified structural equations, while [15] developed a full geometric model of the pulley–winding system, reducing the trajectory tracking error of an additive manufacturing CDPR to 0.4 mm. In [16], a high-precision adaptive control scheme was proposed to improve tracking accuracy. Other studies have employed external visual sensors [17]; for example, [18] demonstrated a position-based visual servo control method using multiple cameras, achieving a maximum position error of less than 1 cm and an orientation error below 0.5°. Most existing designs are based on approximately flat and fixed ground, with operations less affected by terrain and other factors. However, the aforementioned accuracy compensation and correction methods do not consider two scenarios:

1) The impact of significant deformation of the equipment due to terrain changes;

2) Kinematic solving of the CDPR induced by the tilt of the equipment base.

The main challenges stem from the complex outdoor terrain where the CDPR used for solar panel array installation features large scale, high load capacity, and a wide workspace. Its structural configuration inherently leads to low overall rigidity, making it susceptible to deformation caused by undulating and locally uneven ground, which in turn significantly impairs

operational accuracy. Additionally, large-angle tilting of the equipment base alters the kinematic solutions of the underactuated cable-driven mechanism, causing deviations in the end-effector's center position. These factors collectively necessitate effective compensation and correction strategies.

This paper addresses the deformation and tilting issues caused by uneven terrain during the handling and installation operations of outdoor mobile 6-DOF high-load and large-scale CDPR. Corresponding deformation correction algorithms and kinematic solutions are designed. Furthermore, to reduce the complexity of the control system, a PDMW process is designed to decompose the original one-time movement into two phases: a Pre-Motion Phase (PMP) and a Synchronous Motion Phase (SMP). A real-time IKRC method is used to perform real-time compensation for position deviations introduced by the under-constrained 4-cable CDPR to improve system accuracy. The proposed robotic system effectively overcomes the challenges of automated operations in complex outdoor terrains for SPA installation and demonstrates enhanced environmental adaptability.

## II. PRELIMINARIES

### A. Structure of robot

The equipment adopts a gantry structure, with dimensions approximately 10 m × 12 m × 9 m (L × W × H). Each of the "legs" on both sides is equipped with 2 sets of tracks, enabling large-range outdoor movement. The payload is a SPA composed of multiple solar panels, with a maximum size of 15 m × 5 m (L × W) and a maximum mass of 1000 kg. The overall structure is shown in Fig.1.
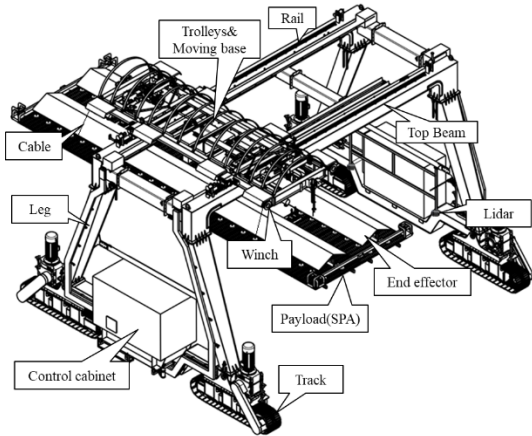


Fig.1. Robot configuration

Three sets of trolleys are serially stacked on the rail of the top beam to form a multi-layer serial mechanism, namely the Y-Trolley, X-Trolley, and Rz-Trolley from bottom to top. Among them, the X-Trolley and Y-Trolley are each driven by a single servo motor to achieve movement in the $X$ and $Y$ directions, respectively; the Rz-Trolley is driven by differential speed of servo motors on both sides to realize movement in the $Y$ direction and rotation around the $\theta_z$ axis.

The moving base is fixedly connected to the Rz-Trolley. Four cables connect the EE to the winches at the four corners of the MB, forming a under-constrained CDPR system, that

enables parallel motion with 4-DOF: $Z$, $\theta_X$, $\theta_y$, and $\theta_z$. Each winch is driven by an independent servo motor.

Due to the lack of active adjustment capability in the $X$ and $Y$ directions of the 4-cable under-constrained CDPR, the multi-layer trolley mechanism can not only achieve realize movements in the $X$, $Y$, and $\theta_z$ directions, but also compensate for the horizontal deviation introduced by the CDPR during motion. Meanwhile, it increases the stroke in the $\theta_z$ direction, thereby enabling the 6-DOF large-scale spatial movement of the EE.

The movement of the Manipulator is jointly realized by the 3 trolleys and the CDPR mechanism. At the bottom of the EE, multiple sets of vacuum suction cups are mounted to adsorb the payload with a maximum mass of 1.2 t, thereby achieving the "grabbing" function. The target pose for handling and installation is positioned using the lidar installed on the "legs".

### B. Kinematics

Firstly, the following coordinate systems are defined: the world coordinate system $\{O_W\}$, the equipment base coordinate system $\{O_B\}$, the Y-Trolley coordinate system $\{O_T\}$, the "leg" coordinate system $\{O_L\}$, the MB coordinate system $\{O_M\}$, the Lidar coordinate system $\{O_{LD}\}$, and the EF coordinate system $\{O_E\}$. All the coordinate systems are shown in Fig.2.
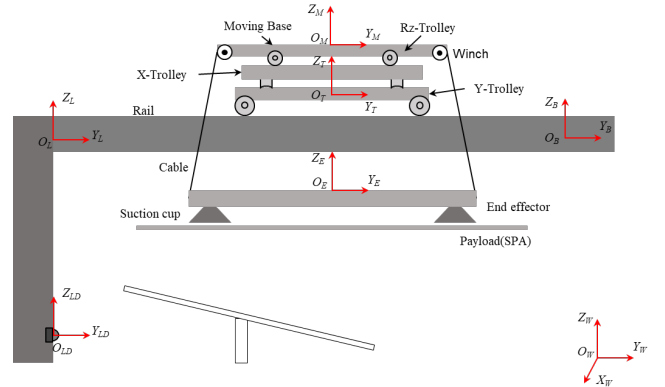


Fig. 2. Coordinate systems of the robot

Table 1. Mechine parameters

| Para. | Value | Definition | Units |
|---|---|---|---|
| $w_E$ | 2.67 | End effector cable anchor points distance on Y-direction | m |
| $l_E$ | 6.78 | End effector cable anchor points distance on X-direction | m |
| $w_M$ | 1.34 | Moving base cable anchor points distance on Y-direction | m |
| $l_M$ | 6.78 | Moving base cable anchor points distance on X-direction | m |
| $m_e$ | 2000 | End effector mass | kg |
| $m'_e$ | 2800 | Sum of end effector mass and payload mass | kg |
| $L_r$ | 6.0 | Y-Trolley rail length | m |
| $L_T$ | 6.7 | Rz-Trolley dual rollers distance on X-direction | m |
| $Z_M$ | 0.5 | Moving base center and Y-Trolley center distance on Z-direction | m |
| $Z_{LD}$ | 5.5m | Lidar center and Leg coordinate center distance on Z-direction | m |

The origin of the $\{O_B\}$ coordinate system is located at the center of the top beam. In the initial state of the equipment, all motors are at their zero positions, and except for the world coordinate system $\{O_W\}$, there is only translation between the internal coordinate systems of the equipment. The main mechanism parameters of the equipment are shown in Table 1.

The target pose of the EE is measured by the lidar, which is expressed in the coordinate system $\{O_{LD}\}$ as $\left[{}^{LD}\boldsymbol{p}_o, {}^{LD}\boldsymbol{\theta}_o\right]$. For subsequent control, the target pose is first transformed into the base coordinate system $\{O_B\}$ as follows:

$$ {}^{B}\mathbf{T}_o = {}^{B}\mathbf{T}_L \, {}^{L}\mathbf{T}_{LD} \, {}^{LD}\mathbf{T}_o, \tag{1} $$

where ${}^{B}\mathbf{T}_L$ and ${}^{L}\mathbf{T}_{LD}$ are the transformation matrices from $\{O_L\}$ to $\{O_B\}\}$ and from $\{O_{LD}\}$ to $\{O_L\}$, respectively.

Since the CDPR is located on the MB, the pose is further transformed into the $\{O_M\}$ coordinate system as follows:

$$ {}^{M}\mathbf{T}_o = {}^{T}\mathbf{T}_M{}^{-1} \, {}^{B}\mathbf{T}_T{}^{-1} \, {}^{B}\mathbf{T}_o, \tag{2} $$

where ${}^{B}\mathbf{T}_T$ and ${}^{T}\mathbf{T}_M$ are the transformation matrices from $\{O_T\}$ to $\{O_B\}$ and from $\{O_M\}$ to $\{O_T\}$, respectively.

In an ideal state, the kinematic solution of the CDPR can be performed based on the aforementioned ${}^{M}\mathbf{T}_o$. However, in the serial-parallel hybrid mechanism of this design, both ${}^{B}\mathbf{T}_T$ and ${}^{T}\mathbf{T}_M$ are driven by their corresponding mechanisms, making them variable matrices. Therefore, it is necessary to reasonably design algorithms and processes for decoupling. Meanwhile, when the equipment is deformed, the above-mentioned constant matrices will also change, requiring correction to ensure the final solution accuracy.

## III. METHOD

Due to the gantry configuration, heavy payload, and large footprint, uneven terrain can induce deformation of the top beam and rail in forms such as arching, sagging, and twisting, as illustrated in Fig. 3. In this section, the deformation compensation mechanism and decoupling control method based on inverse kinematics are presented.
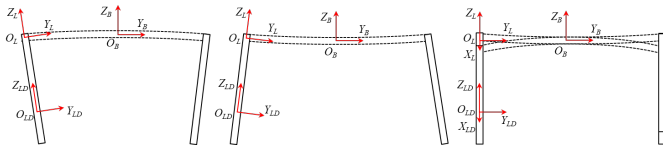
### A. Deformation Compensation



Fig.3. Top beam deformations: a) arching, b) sagging, and c) twisting

The gantry "legs," designed as an integrated and high-rigidity structure, experience negligible deformation. That is, ${}^{L}\mathbf{T}_{LD}$ is guaranteed by the design and remains unaffected by terrain conditions:

$$ {}^{L}\mathbf{T}_{LD} = \begin{bmatrix} \mathbf{I} & [0,0,\boldsymbol{Z}_{LD}]^T \\ \mathbf{0} & 1 \end{bmatrix}, \tag{3} $$

where $\boldsymbol{Z}_{LD}$ is the Z-direction distance from the radar center to the center of the "leg" base coordinate system $\{O_L\}$, which is an equipment parameter.

In contrast, both ${}^{B}\mathbf{T}_L$ in (1) and ${}^{B}\mathbf{T}_T$ in (2) vary with terrain unevenness. The transformation ${}^{B}\mathbf{T}_L$ can be directly obtained by the lidar through point cloud matching using the feature points of the "legs", however, ${}^{B}\mathbf{T}_T$ depends on both the Y-trolley position and top beam deformation, making it inaccessible via direct measurement. Fig.4 illustrates the Y-Trolley path and the deformation of the rail.
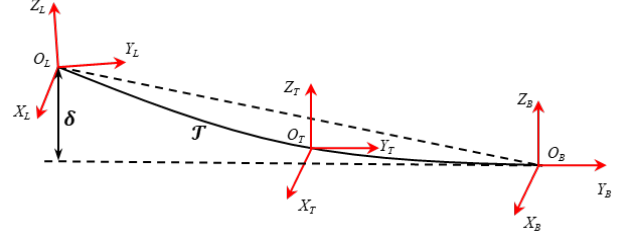


Fig.4. The Y-Trolley path $\mathcal{T}$ and the deformation $\boldsymbol{\delta}$ of the rail

Experimental measurements indicate that the maximum crossbeam deformation satisfies $max(\|\boldsymbol{\delta}\|) < 0.2\text{m}$, which is mainly concentrated in the Z direction. Under this condition:

$$ L(\mathcal{T}) \approx \left\| {}^{B}\boldsymbol{p}_L \right\|, \tag{4} $$

where ${}^{B}\boldsymbol{p}_L$ is the position vector associated with ${}^{B}\mathbf{T}_L$.

When the Y-Trolley moves along the rail, the component ${}^{B}y_T$ in the position vector ${}^{B}\boldsymbol{p}_T = [{}^{B}x_T, {}^{B}y_T, {}^{B}z_T]^T$ can be replaced by the encoder feedback position ${}^{B}y_{encoder}$, while the trajectories of ${}^{B}x_T$ and ${}^{B}z_T$ approximate a parabola. Exploiting this property, a MNIP algorithm is proposed for deformation estimation, where quadratic interpolation is applied to ${}^{B}\boldsymbol{p}_T$, and quaternion interpolation is applied to ${}^{B}\boldsymbol{\theta}_T$. The position vector ${}^{B}\boldsymbol{p}_T$ is obtained through quadratic curve fitting as

$$ {}^{B}\boldsymbol{p}_T = \begin{bmatrix} a_x \, {}^{B}x_T{}^2 + b_x \\ {}^{B}y_{encoder} \\ a_z \, {}^{B}z_T{}^2 + b_z \end{bmatrix}, \tag{5} $$

$$ s.t. \begin{cases} {}^{B}\boldsymbol{p}_T|_{t=0} = {}^{B}\mathbf{0} \\ {}^{B}\boldsymbol{p}_T|_{t=t_e} = {}^{B}\boldsymbol{p}_L \end{cases}, $$

among them, $a_x$, $a_z$, $b_x$ and $b_z$ are the corresponding fitting coefficients, which are calculated based on boundary conditions.

The attitude vector ${}^{B}\boldsymbol{\theta}_T$ corresponding to the transformation matrix ${}^{B}\mathbf{T}_T$ can be obtained via quaternion Spherical linear interpolation (SLERP):

$$ \begin{cases} \theta = \arccos\left( {}^{B}\boldsymbol{q}_0 \cdot {}^{B}\boldsymbol{q}_L \right) \\ \lambda = \dfrac{|y_B|}{\frac{L_r}{2}}, \quad y_B \in \left[-\frac{L_r}{2}, \frac{L_r}{2}\right] \\ {}^{B}\boldsymbol{q}_T = \dfrac{\sin(\theta(1-\lambda))}{\sin\theta} {}^{B}\boldsymbol{q}_0 + \dfrac{\sin(\theta\lambda)}{\sin\theta} {}^{B}\boldsymbol{q}_L \end{cases}, \tag{6} $$

where ${}^{B}\boldsymbol{q}_0 = (1,0,0,0)$ is the unit quaternion corresponding to ${}^{B}y_T = 0$, ${}^{B}\boldsymbol{q}_L$ is the quaternion corresponding to ${}^{B}\boldsymbol{\theta}_L(t)$, ${}^{B}\boldsymbol{q}_T$ is the quaternion corresponding to ${}^{B}\boldsymbol{\theta}_T$.

Using (5) and (6), the corrected transformation matrix ${}^{B}\mathbf{T}_T$ can be determined. Subsequently, the corrected ${}^{M}\mathbf{T}_o$ is derived

from (1) and (2), corresponding to the pose $[^M\boldsymbol{p}_o, {}^M\boldsymbol{\theta}_o]$, which is subsequently incorporated into the inverse kinematics framework to achieve motion decoupling between translational and rotational degrees of freedom. This integration ensures that the cable length solutions account for structural deformations, thereby preventing trajectory drift and orientation misalignment of the EE. By isolating the deformation-induced displacement components from the intended motion commands, the control system is able to maintain high positioning accuracy even under substantial crossbeam distortion.

### B. CDPR Inverse Kinematics

The MB and the EE form an independent CDPR system, which can be analyzed for motion separately. Unless otherwise specified, all coordinates in this section are relative to the MB coordinate system $\{O_M\}$. Fig.5. are top view of the CDPR .
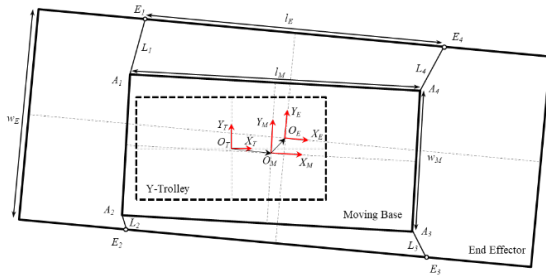


Fig.5. Top view of the CDPR

The position and attitude of the EE can be represented by a rotation matrix $\mathbf{R}$ and a translation vector $\boldsymbol{p}$. The rotation matrix $\mathbf{R}$ is determined by the attitude angles $(\theta_x, \theta_y, \theta_z)$. The position vector of the connection point $\boldsymbol{E}_i$ between the EE and the cable in the coordinate system $\{O_M\}$ is given by

$$\boldsymbol{r}_i = \boldsymbol{p} + \mathbf{R}r_i'. \tag{7}$$

The length $L_i$ of each cable can be calculated using the position of the cable on the moving base and the fixed point $A_i$ of the cable:

$$L_i = \|\boldsymbol{A}_i - \boldsymbol{r}_i\|. \tag{8}$$

The corresponding direction vector of the cable is

$$\boldsymbol{u}_i = \frac{\boldsymbol{A}_i - \boldsymbol{r}_i}{L_i}. \tag{9}$$

The cable force $T_i$ is transmitted along the direction vector $\boldsymbol{u}_i$. And the force balance and moment balance conditions for the EE are expressed as

$$\begin{cases} \sum_{i=1}^{4} T_i \boldsymbol{u}_i + \mathbf{F}_{ext} = 0 \\ \sum_{i=1}^{4} T_i (\boldsymbol{r}_i \times \boldsymbol{u}_i) + \mathbf{M}_{ext} = 0 \end{cases}, \tag{10}$$

where $\mathbf{F}_{ext}$ and $\mathbf{M}_{ext}$ are the resultant external force and resultant external moment acting on the EE, respectively, and $\mathbf{F}_{ext} = m_e'\boldsymbol{g} = m_e'[0\ 0 - g]^T$.

During outdoor operations, ground slopes may cause the moving base coordinate system $\{O_M\}$ to tilt with respect to the world coordinate system $\{O_W\}$, resulting in a misalignment between the gravity direction and the Z-axis of $\{O_M\}$. This misalignment alters both $\mathbf{F}_{ext}$ and $\mathbf{M}_{ext}$, thereby necessitating a gravity compensation process to maintain accurate force and moment equilibrium of the EE:

$$\boldsymbol{g}' = {}^W\mathbf{R}_B \boldsymbol{g} = {}^W\mathbf{R}_B \begin{bmatrix} 0 \\ 0 \\ -g \end{bmatrix}, \tag{11}$$

where ${}^W\mathbf{R}_M$ is the rotation matrix of $\{O_M\}$ relative to $\{O_w\}$, measured by the IMU installed at the center of the MB. The external force $\mathbf{F}_{ext}$ and external moment $\mathrm{M}_{ext}$ are corrected as follows:

$$\begin{cases} \mathbf{F}_{ext} = m_e'\mathbf{g}' \\ \mathbf{M}_{ext} = \boldsymbol{r}_c \times (m_e'\boldsymbol{g}')' \end{cases} \tag{12}$$

where $\boldsymbol{r}_c$ is the position vector of the spreader's center of gravity in $\{O_M\}$.

The aforementioned equations (7-9), (11) and (12) are combined to form a system of geometric constraints and static equilibrium equations. Given the input target pose $[z, \theta_x, \theta_y, \theta_z]$ in $\{O_M\}$, numerical optimization methods can be used to solve for $[dx, dy, l_1, l_2, l_3, l_4, F_1, F_2, F_3, F_4]$. Here, $dx$ and $dy$ capture the horizontal offsets of the $\{O_E\}$ center relative to the $\{O_M\}$ coordinate center introduced by the under-constrained CDPR, while $l_i$ and $F_i$ are the lengths and tensions of each cable, respectively.

### C. Trolley Inverse Kinematics

To achieve precise and decoupled control of the CDPR system, it is essential to analyze the kinematics of the trolley mechanisms that support and drive the MB. All poses in this section are relative to the coordinate system $\{O_T\}$, and the top view of the trolleys is shown in Fig.6.
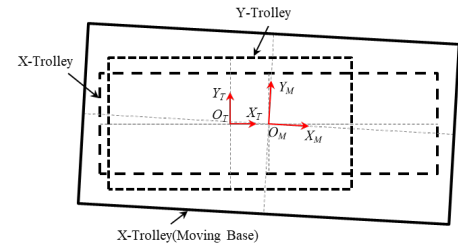


Fig.6. Top view of the trolleys

The kinematic relationship of the trolley system is expressed as

$$\begin{cases} \boldsymbol{p} = [x, y, z]^T \\ \boldsymbol{\theta} = [0,0, \theta_z]^T \end{cases}, \tag{13}$$

$$s.t. \quad z = \boldsymbol{Z}_M,$$

where x is the displacement of the X-Trolley, and $y$ and $\theta_z$ are the displacements of the center of the moving base in the $Y$ and $\theta_z$ directions in $\{O_T\}$, respectively. Let the bilateral motors of the Rz-Trolley be Y1 and Y2, then

$$\begin{cases} y = \frac{y_1 + y_2}{2} \\ \theta_z = \frac{y_1 - y_2}{L_T} \end{cases}, \tag{14}$$

where $y_1$ and $y_2$ are the displacements corresponding to the Y1 and Y2 motors, respectively.

Since both the CDPR and the MB mechanism can achieve $\theta_z$ movement, to simplify decoupling control, the $\theta_z$ displacement of the CDPR is set to 0, and the Rz-Trolley movement is restricted to the $\theta_z$ direction to maximize the movement stroke of the EE in the $\theta_z$ direction. Thus, equation (14) is modified as

$$\begin{cases} \frac{y_1+y_2}{2} = 0 \\ \theta_z = \frac{y_1-y_2}{L} \end{cases}, \tag{15}$$

Thus, the displacements corresponding to motors Y1 and Y2 can be solved according to the input $\theta_z$.

### D. Control

To address deformation compensation and ground slope correction, a dedicated PDMW is designed to reduce mutual coupling and control complexity. This workflow decomposes the manipulation of the robot into two steps: 1) The PMP, implemented by the three trolleys; 2) The SMP, achieved by the synchronous movement of the CDPR and trolleys.

During the PMP, the X-Trolley, Y-Trolley, and Rz-Trolley each move independently to their target positions based on $^Bx$, $^By$ and $^B\theta_z$ derived from the initial $^{LD}T_o$. In the SMP, the under-constrained nature of the CDPR induces additional deviations $dx$ and $dy$ of $\{O_E\}$ relative to $\{O_M\}$. Since both these deviations are smaller than the maximum stroke of the X-Trolley and Y-Trolley, they can be eliminated through real-time IKRC by the X-Trolley and Y-Trolley, thereby achieving accurate 6-DOF motion control of the EE. To facilitate the explanation of the compensation mechanism, the control block diagram of the SMP is provided in Fig. 7. The block diagram for the PMP is analogous and therefore omitted for brevity.
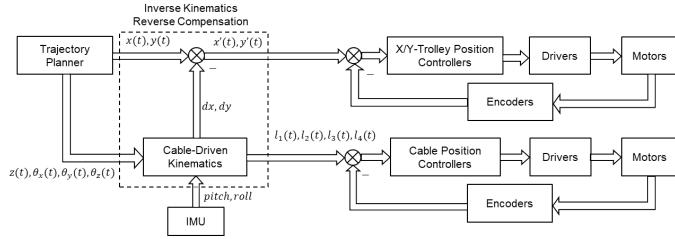


Fig.7. SMP control framework

Each motor driver operates in speed control mode, with position control implemented through standard PID controllers. The planner module performs trajectory planning in the Cartesian coordinate system, taking into account the 6-DOF target pose as well as maximum velocity and acceleration constraints for each axis.

## IV. PERFORMANCE AND RESULTS

Algorithm verification was conducted to simulate the positional offsets of the EE induced by the under-constrained CDPR under varying ground slope conditions. As shown in Fig.8(a), when there is no ground undulation, the equipment maintains a horizontal working state. For the target attitude with $|\theta_x| = 40°$, $|\theta_y| = 10°$, and $\theta_z = 0°$, $dx$ and $dy$ can reach 0.075 m and 0.211 m, respectively. Fig.8(b) shows that under sloped ground conditions that induce pitch and roll angles of -10° and

5°, the maximum $dx$ and $dy$ can reach 0.22 m and 0.543 m, respectively. The results verified the effectiveness of the IKRC.
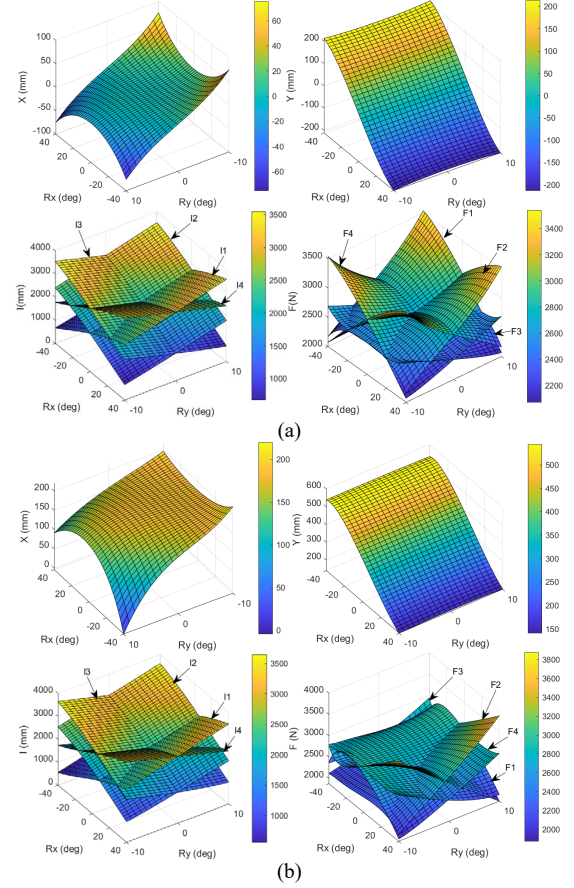


Fig.8. Results of CDPR inverse solution under the conditions of $m'_e = 800\ kg$, $z = -2.0$ m, $\theta_z = 0°$, $\theta_x \in [-40°, 40°]$, $\theta_y \in [-10°, 10°]$: a) Horizontal ground, with both the pitch angle and roll angle of the equipment being 0°; b) Sloped ground, with the equipment having a pitch angle of -10° and a roll angle of 5°.



Fig.9. The SPA installation robot and outdoor desert terrain

MNIP primarily employs parabolic interpolation and quaternion SLERP interpolation, resulting in low computational complexity. Under the configuration of an IPC with an i9 processor, 32GB of memory, and the Ubuntu 24.04 system, the computation time of MNIP is less than 1ms, and that of IKRC is less than 13ms, which satisfies the 20Hz control cycle.

Fig. 9 presents the actual robot test scenarios and the outdoor desert terrain. The maximum terrain unevenness within the equipment's footprint reaches 0.5 m, causing considerable structural deformation of the equipment. Considering a SPA with dimensions of 15.5 m × 4.5 m (L × W) and a mass of

800 kg, the equipment exhibits pitch and roll angles of 2.11° and 0.35°, respectively. The target pose of the EE of $[x, y, z, \theta_x, \theta_y, \theta_z] =$
$[0.158\,m, -2.219\,m, -1.955\,m, 0.361°, -0.067°, -1.135°]$ . Measurement results after multiple executions of the PDMW method, both before and after applying the MNIP deformation compensation and IKRC correction, are shown in Fig. 10.
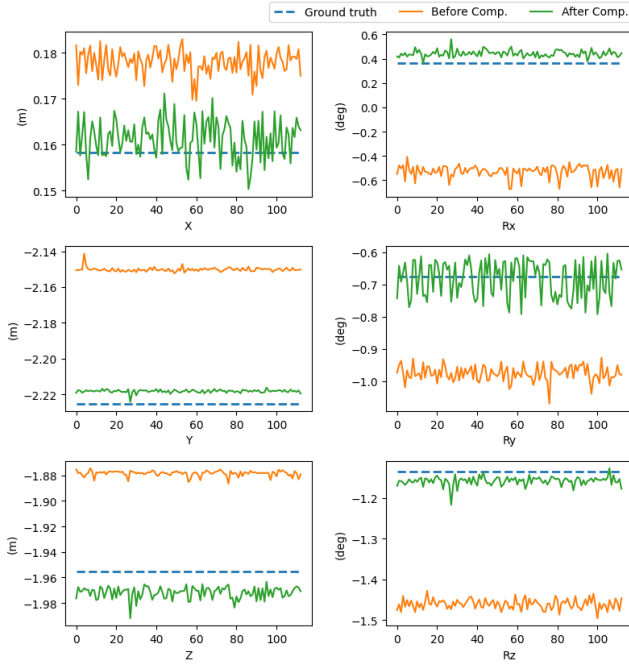


Fig.10. Comparison of 6-DOF accuracy before and after compensation and correction with decoupled control

It can be seen that before compensation and correction, the absolute values of the deviations between the actual final pose and the target pose are $|\overline{\boldsymbol{\delta}}| = [\bar{\delta}_x, \bar{\delta}_y, \bar{\delta}_z, \bar{\delta}_{\theta_x}, \bar{\delta}_{\theta_y}, \bar{\delta}_{\theta_z}]^T =$ $[0.019\,m, 0.075\,m, 0.077\,m, 0.89°, 0.3°, 0.325°]^T$ . After compensation and correction, the average deviations reduce markedly to $|\overline{\boldsymbol{\delta}}'| = [\bar{\delta}_x{'}, \bar{\delta}_y{'}, \bar{\delta}_z{'}, \bar{\delta}_{\theta_x}{'}, \bar{\delta}_{\theta_y}{'}, \bar{\delta}_{\theta_z}{'}]^T =$ $[0.003\,m, 0.007\,m, 0.017\,m, 0.08°, 0.007°, 0.023°]$ . The deviations of each DOF are significantly reduced, with the variance being $\boldsymbol{\sigma} = [\sigma_x, \sigma_y, \sigma_z, \sigma_{\theta_x}, \sigma_{\theta_y}, \sigma_{\theta_z}]^T =$ $[0.004\,m, 0.001\,m, 0.004\,m, 0.027°, 0.056°, 0.011°]$ , which meets the system accuracy requirements.

To the best of our knowledge, there is very limited literature addressing CDPR-based installation of large-scale solar panel arrays. Prior studies on CDPRs for construction or aerospace assembly report positioning accuracies in the range of 10-50 mm for payloads up to 250-400 kg. However, these robots mostly adopt more expensive and precise measurement systems, which results in limited environmental adaptability. Our system, designed for SPAs up to 1.2 t, uses a more universal and low-cost lidar as the positioning system, and can achieve comparable or better accuracy (30-50 mm) while handling larger distributed loads in more complex environments, demonstrating the feasibility of CDPRs for this new application.

## V. CONCLUSION

This paper develops a 6-DOF high-load robot designed for outdoor SPA installation, integrating a 4-cable under-constrained CDPR with a multi-layer serial motion mechanism. By incorporating equipment tilt caused by ground slopes into the inverse kinematics of the under-constrained CDPR, the system compensates for pose variations induced by uneven terrain. A deformation correction method based on MNIP is applied to address structural distortions due to terrain unevenness, thereby improving operational accuracy. Additionally, a dedicated PDMW and IKRC method are introduced to simplify the control system and achieve effective motion decoupling. Experimental results from outdoor desert environments with ground slopes less than 10° and local terrain unevenness up to 0.5 m demonstrate that the robot attains operational accuracy between 0.03 m and 0.05 m when installing SPAs measuring 15.5 m by 4.5 m with a mass of approximately 800 kg. These findings confirm the system's capability to enhance installation precision and its adaptability for diverse indoor and outdoor application scenarios.

Since the designed maximum payload of the SPA installation robot is 1.2 t, exceeding this mass may result in failure of the EE to handl the payload or damage to the robot mechanism, thus requiring a redesign of the EE or an improvement in the mechanism strength. For payloads with a mass of less than 1.2 t and dimensions of less than 15 m × 5 m (L × W), the robot can manipulate normally, and all the proposed methods are applicable. If the mass is less than 1.2 t but the dimensions are exceeded, the EE also needs to be redesigned.

## REFERENCES

[1] P. Vähä, T. Heikkilä, P. Kilpeläinen, et al., "Extending automation of building construction—Survey on potential sensor technologies and robotic applications," Autom. Constr., vol. 36, pp. 168–178, 2013.

[2] K. Iturralde, M. Feucht, D. Illner, et al., "Cable-driven parallel robot for curtain wall module installation," Autom. Constr., vol. 138, p. 104235, 2022.

[3] T. P. Tho and N. T. Thinh, "Using a cable-driven parallel robot with applications in 3D concrete printing," Appl. Sci., vol. 11, no. 2, p. 563, 2021.

[4] Z. Zhang, Z. Shao, Z. You, et al., "State-of-the-art on theories and applications of cable-driven parallel robots," Front. Mech. Eng., vol. 17, no. 3, p. 37, 2022.

[5] M. Zarebidoidi, J.S. Dhupia, and W. Xu, "A review of cable-driven parallel robots: Typical configurations, analysis techniques, and control methods," IEEE Robot. Autom. Mag., vol. 29, no. 3, pp. 89–106, 2022.

[6] Pott, C. Meyer, and A. Verl, "Large-scale assembly of solar power plants with parallel cable robots," in Proc. ISR 2010 (41st Int. Symp. Robot.) and ROBOTIK 2010 (6th German Conf. Robot.), VDE, 2010, pp. 1–6.

[7] M. Fabritius, P. Miermeister, W. Kraus, et al., "A framework for analyzing the accuracy, complexity, and long-term performance of cable-driven parallel robot models," Mech. Mach. Theory, vol. 185, Art. no. 105331, 2023.

[8] Martin, M. Fabritius, J. T. Stoll, et al., "Accuracy improvement for CDPRs based on direct cable length measurement sensors," in Proc. Int. Conf. Cable-Driven Parallel Robots, Cham, Switzerland: Springer Int. Publishing, 2021, pp. 348–359.

[9] Schmidt and A. Pott, "Increase of position accuracy for cable-driven parallel robots using a model for elongation of plastic fiber ropes," in New Trends in Mechanism and Machine Science: Theory and Industrial Applications, Cham, Switzerland: Springer Int. Publishing, 2016, pp. 335–343.

[10] M. Fabritius and A. Pott, "An inverse kinematic code for cable-driven parallel robots considering cable sagging and pulleys," in Proc. Eur. Conf. Mechanism Science, Cham, Switzerland: Springer Int. Publishing, 2020, pp. 423–431.

[11] M.R. Dindarloo, A.S. Mirjalili, S.A. Khalilpour, et al., "A graph-based self-calibration technique for cable-driven robots with sagging cable," in Proc. IEEE/RSJ Int. Conf. Intell. Robots Syst. (IROS), 2024, pp. 872–877.

[12] R. Yao, H. Li, and X. Zhang, "A modeling method of the cable driven parallel manipulator for FAST," in Cable-Driven Parallel Robots, Berlin, Heidelberg: Springer Berlin Heidelberg, 2012, pp. 423–436.

[13] H. Li, "A giant sagging-cable-driven parallel robot of FAST telescope: its tension-feasible workspace of orientation and orientation planning," in Proc. 14th IFToMM World Congr., 2015, pp. 373–381.

[14] Pott, "Influence of pulley kinematics on cable-driven parallel robots," in Latest Advances in Robot Kinematics, Dordrecht, Netherlands: Springer Netherlands, 2012, pp. 197–204.

[15] Zhang, W. Shang, B. Deng, et al., "High-precision adaptive control of cable-driven parallel robots with convergence guarantee," IEEE Trans. Ind. Electron., vol. 71, no. 7, pp. 7370–7380, 2023.

[16] Gueners, H. Chanal, and B. C. Bouzgarrou, "Design and implementation of a cable-driven parallel robot for additive manufacturing applications," Mechatronics, vol. 86, p. 102874, 2022.

[17] M. Pinto, E. Moreira, J. Lima, et al., "A cable-driven robot for architectural constructions: a visual-guided approach for motion control and path-planning," Auton. Robots, vol. 41, no. 7, pp. 1487–1499, 2017.

[18] T. Dallej, M. Gouttefarde, N. Andreff, et al., "Modeling and vision-based control of large-dimension cable-driven parallel robots using a multiple-camera setup," Mechatronics, vol. 61, pp. 20–36, 2019.